Integration of COSMO-SkyMed and GeoEye-1 Data With Object-Based Image Analysis

M. Gianinetto, M. Rusmini, A. Marchesi, P. Maianti, F. Frassy, G. Dalla Via,
L. Dini, *Member, IEEE*, and F. Rota Nodari

I. Introduction

According to the Committee on Earth Observation Satellites, about 300 satellites for Earth observation were launched in the last 50 years and more than 200 are planned over the next 15 years [1]. In this scenario, the interest for multisource integration rapidly increased in the scientific community, especially for mixing together data gathered with imaging sensors in the optical and microwave domains [2]–[6]. With respect to land-cover/land-use (LC/LU) mapping, the information provided by multispectral (MS) images are useful for identifying LC/LU classes according to their spectral signature and geometry, whereas synthetic aperture radar (SAR) data give information about surface roughness, soil moisture, object shape, and orientation. Besides, SAR sensors are able to collect information all-weather, day, and night, thus increasing the temporal resolution of optical sensors those observation capabilities are limited by weather conditions and cloud cover.

After entering the era of commercial very high-resolution (VHR) imaging from space at the beginning of the 21st century with the first MS satellites (Ikonos and QuickBird), the advent of VHR X-band SAR space sensors [COSMO-SkyMed (CSK®) and TerraSAR-X] widened the interest of multisource data integration for LC/LU map to the VHR domain [7]–[13]. On the one hand, VHR imagery gives the possibility to describe LC/LU classes with more detail than low- and medium-resolution data: spatial extent, shape, structure, and texture of landscape features appear clearer because the mixture of different classes in a single pixel is directly proportional to the pixel size [14]. On the other hand, moving from medium to high resolution, the internal variability of LC/LU classes increases, leading to an overall decrease of accuracy in pixel-based (PB) classification because geometric and semantic information are absent in single images pixels [15]–[17].

Object-based image analysis (OBIA) aims at grouping adjacent image pixels into self-existent objects (or segments) with spectral and geometric similarities, so that textural and contextual/relational characteristics among objects can be exploited as well in thematic classification [18], [19]. Better results of OBIA approaches in LC/LU mapping compared to PB analyses have been widely demonstrated, especially with VHR optical data [16], [20]. Furthermore, OBIA allows the assimilation of optical images with other kind of data, such as LiDAR [21], [22], asserting itself as a powerful tool for multisource data integration. The authors describing OBIA approaches usually distinguish between urban and agricultural/natural LU/LC classification, because features are remarkably different with respect to their size, geometry, and patterns [20], [23]–[25]. When dealing with single-band images, like panchromatic or single polarization SAR, textural measurements and local spatial statistics may be used to increase the classification accuracy. For example, [26] improved riparian ecosystem classification by using textural information derived from VHR optical images and [27] improved OBIA classification in urban areas by adding gray-level cooccurrence measures (GLCM) and Moran's I spatial statistics to VHR MS data.

Manuscript received September 02, 2014; revised April 09, 2015; accepted April 13, 2015. Date of publication May 14, 2015; date of current version July 20, 2015. This work was supported by the Italian Space Agency under Grant I/042/09/0 "Evaluation of COSMO-SkyMed system and performances and simulation of future ORFEO system with existing optical data." COSMO-SkyMed data were provided by the Italian Space Agency.

M. Gianinetto, A. Marchesi, P. Maianti, F. Frassy, and F. Rota Nodari are with the Laboratory of Remote Sensing (L@RS), Department of Architecture, Built Environment, and Construction Engineering (ABC), Politecnico di Milano, Milano 20133, Italy (e-mail: marco.gianinetto@polimi.it; andrea.marchesi@polimi.it; pieralberto.maianti@polimi.it; federico.frassy@polimi.it; francesco.rotanodari@polimi.it).

M. Rusmini was with the Laboratory of Remote Sensing (L@RS), Department of Architecture, Built Environment, and Construction Engineering (ABC), Politecnico di Milano, Milano 20133, Italy. He is now with the ERM Italia S.p.A., Milano 20124, Italy (e-mail: marco.rusmini@erm.com).

G. Dalla Via was with the Laboratory of Remote Sensing (L@RS), Department of Architecture, Built Environment, and Construction Engineering (ABC), Politecnico di Milano, Milano 20133, Italy. He is now with the Istituto Nazionale di Geofisica e Vulcanologia–Sezione di Milano, Milano 20133, Italy (e-mail: giorgio.dallavia@ingv.it).

L. Dini is with the Space Geodesy Center of the Italian Space Agency (ASI), Matera 75100, Italy (e-mail: luigi.dini@asi.it).

Color versions of one or more of the figures in this paper are available online.

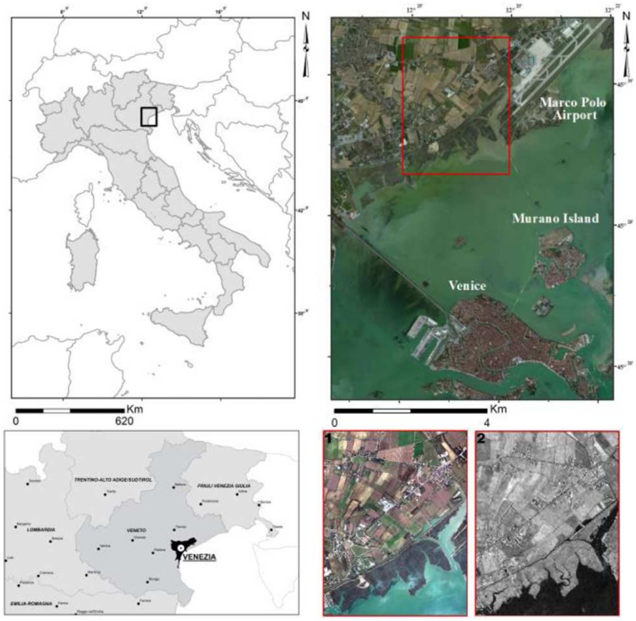

Fig. 1. Study area and data. 1) GE1 MS image (true colors). 2) CSK® amplitudes (data provided by the Italian Space Agency).

Other studies exploited first-order and second-order textural measurements to improve urban LC/LU classification with either MS or SAR VHR images [28], [29].

Past studies suggested that the incorporation of synthetic aperture data could improve the LC/LU mapping based on optical images. However, most of the literature considered medium-resolution data, typically Landsat-TM or SPOT for optical and RADARSAT or ERS for radar. At present, only few studies reported case histories of thematic classification involving both MS and SAR images collected with metric or submetric spatial detail [7], [8], [10], [11], [13], [30], [31]. Furthermore, most of them debated the mapping in urban areas or in natural areas and only few managed both LC/LU in the same classification workflow.

The main objective of this study is to fill this gap, by assessing the classification's improvement of VHR MS satellite images of a complex environment made up of both urban and rural areas by incorporating in the classification workflow single-polarization X-band SAR data, like CSK® [32], without the need of developing *ad hoc* algorithms. The expected benefit of including the SAR information is to achieve a better knowledge of the LC/LU fragmentation.

II. METHODS

A. Study Area and Data

The study area is located near the Marco Polo Airport, on the shore of the Venetian Lagoon, west of Veneto region in the North–West Italy (Fig. 1). Originally dominated by agriculture, in the last decade, the test site has been partially urbanized and nowadays it shows an intricate mixture of settlements, cultivations, channels, roads, and marshes. Therefore, the site provides a suitable research area for examining LC/LU mapping in a complex environment.

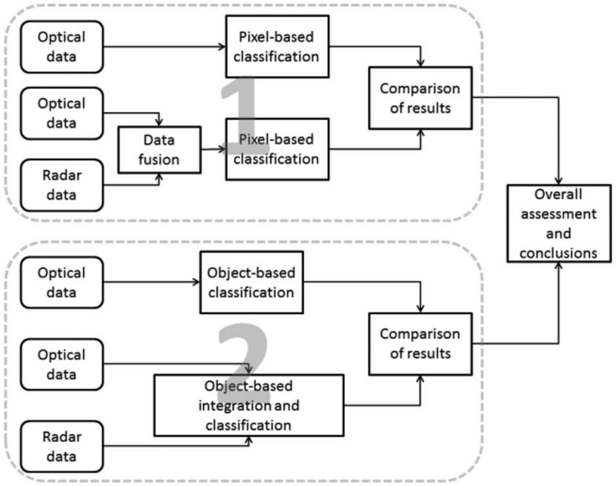

Fig. 2. Outline of the processing and analysis workflow. 1) PB data fusion and classification. 2) Data integration with OBIA.

VHR optical images were acquired over the Venetian Lagoon on February 12, 2010 with GeoEye-1 (GE1). GE1 images were taken with a nominal collection elevation of 73.2°, resulting in a nominal spatial resolution of 0.43 m for the panchromatic channel and 1.74 m for the four-band MS. The data were supplied as geo product without dynamic range adjustment and resampled with nearest neighbor to standard 0.5 m for panchromatic and 2.0 m for MS.

The radar data were an X-band CSK® image acquired over the Venetian Lagoon on March 27, 2010 and part of a stack made up of 61 CSK images collected by the Italian Space Agency in the framework of its announcement of opportunity on the demonstration of the COSMO-SkyMed capabilities and exploitation for science and civilian applications. The data used in this study were an ascending, single-polarization, HH-mode, Stripmap scene, with a nominal spatial resolution of 3.0 m.

B. Classification Schemes

The benefit of the data integration of the X-band SAR information for LC/LU mapping was evaluated in two stages. Fig. 2 outlines the processing and analysis workflow.

First, a standard PB classification was performed with GE1 MS data and the maximum likelihood algorithm. The following classes were defined: 1) Arable land; 2) tile roofs; 3) gray roofs; 4) paved surfaces; 5) bare soil; 6) beet; 7) wheat/barley; 8) forest; 9) grassland; 10) marshes; 11) roads; and 12) water. Training samples were collected with an equalized random sampling scheme [33]: for each land-cover class, about 1000 random samples were extracted. During postclassification, "tile roofs," "gray roofs," and "paved surfaces" were merged into the superclass "built-up." The same classification scheme aforementioned (same algorithm, same classes, same training samples) was applied to GE1 and CSK® fused data.

The second stage was object-based (OB) classifications of the study area, first executed with only GE1 imagery and then with both GE1 and CSK data, where GE1 spectral signatures were coupled with CSK amplitude values and texture features calculated with GLCMs. In this case, training samples (here objects) were generated from those used in the PB classification [34]. For example, the training objects for the class "vegetated" were a subset of the training samples from the classes "forest," "grassland," "marshes," and "wheat/barley" used in the PB classification.

Finally, validation was performed based on equalized random sampling: for each LC/LU class, 200 testing samples were generated and tested.

The standard preprocessing of CSK data was performed by Tele-Rilevamento Europa, the data processing of GE1 and the PB thematic classifications was done using Exelis' IDL/ENVI, DWT was performed with IDL [35], and Trimble's e-Cognition was used for the OBIA.

C. Data Preprocessing

Focusing, despeckling, equalization, and projected to the UTM-WGS84 reference system were applied to CSK® raw data as standard data preprocessing [36], [37]. Since standard procedures are not enough for making SAR data suitable for the integration with optical imagery with already available methods and software, the speckle-free CSK® amplitude distribution was compressed and clipped for making it comparable to GE1 data distribution, thus avoiding computational issues during data fusion and image classification. According to (1), the long right tale of the CSK data was compressed

$$A_{\log} = \log_{10}\left[A_0 + (1 - \min_{A_0})\right] \tag{1}$$

where A_0 is the original CSK® amplitude signal and $A_{\log}$ is the log-transformed CSK® amplitude signal.

To further reconcile the optical and SAR data distributions, a cutoff threshold was applied to $A_{\log}$. The clipping was determined by analyzing the membership of the CSK data to LC/LU classes (Fig. 3): features with extremely large SAR amplitudes mainly belonged to the "built-up" superclass, followed by the classes "Arable land" and "forest." On the other hand, features with extremely small SAR amplitudes mainly belonged to the class "water," followed by shadowed "built-up" areas. By analyzing the rate of change, the left tale of the density function was clipped at 0.6% and the right tale was clipped at 99.0% (Fig. 4). Data values clipped were replaced with the corresponding cutoff level. According to this criterion, features included in the clipped tails mainly belonged to "water" (94.0%) or "built-up" (68.5%). Consequently, the misclassification introduced with the left-side cutoff was 0.04% (6% of 0.6%) and 0.32% for the right-side cutoff (31.5% of 1%). It is negligible if compared to the classification results. Fig. 5 shows CSK® data distribution before and after data preprocessing.

Finally, CSK® data were rescaled to match the dynamic range of GE1 MS images (11 bpp) and the coregistration of the whole data set was fine-tuned using ground control points manually collimated on existing 1:5000 scale topographic maps. GE1 data were preprocessed by applying standard radiometric calibration. Fig. 6 shows an overview of the whole preprocessing.

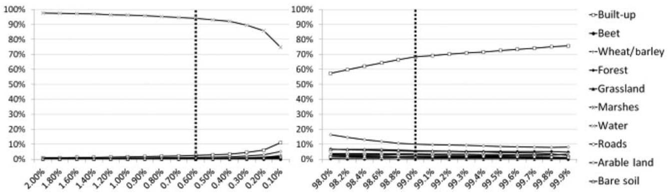

Fig. 3. Membership of the CSK® data to LC/LU classes. *Left*: left tale of the density function. *Right*: right tale of the density function.

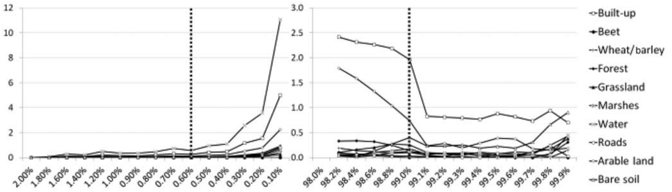

Fig. 4. Rate of change of the membership of the CSK® data to LC/LU classes. *Left*: left tale of the density function clipped at 0.6%. *Right*: right tale of the density function clipped at 99.0%.

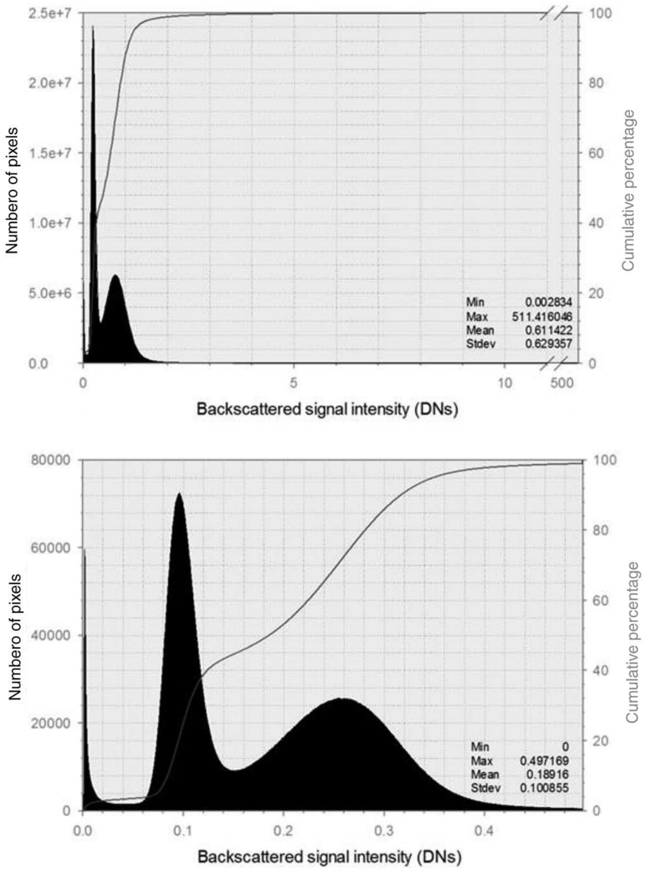

Fig. 5. Histograms of CSK® amplitude values. Top: original data. Bottom: data after log-transformation and clipping.

D. PB Approach

Image fusion aims at integrating data collected with different sensors to obtain more information than what can be gathered from the single sensors. For optical and radar data fusion, the final scope is to summarize in the image pixel the information

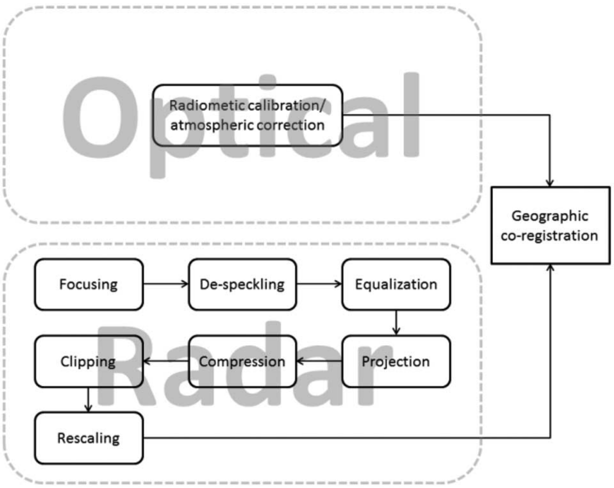

Fig. 6. Preprocessing workflow.

TABLE I
CORRELATION VALUES BETWEEN GE1 AND CSK® FUSED DATA, GE1 SPECTRAL BANDS (MS1–MS4), AND CSK® AMPLITUDE DATA

Method	GE1 MS1	GE1 MS2	GE1 MS3	GE1 MS4	GE1 mean	CSK®
HIS	N/A [a]	–0.11	0.45	0.68	0.48	**0.91**
PC	0.53	0.45	0.51	**0.64**	0.53	0.54
DWT	0.76	**0.82**	0.76	0.80	0.78	0.45

Best results in bold.

[a] N/A, not applicable.

from both the target reflectance in the solar spectrum, related to its physical and biochemical properties, and the backscattering of the SAR signal, related to its texture properties and moisture content.

In this study, three well-established techniques were considered for image fusion: hue-intensity-saturation (HIS) fusion, principal component analysis (PCA), and discrete wavelet transform (DWA) [38]. For each technique, the correlation coefficients between the fused data and the original images were calculated [39]. HIS had a good overall correlation with the CSK® data, but showed poor results with the GE1 due to the high color distortion of the technique. Furthermore, this method is able to fuse only three bands at the same time. PCA and DWT returned better results: PCA was more correlated with CSK® than DWT, which was more faithful to the GE1 data. Based on the results shown in Table I, the DWT method was finally selected and used for thematic classification.

As introduced, both the GE1 image and the fused GE1 + CSK® synthetic data were classified with standard maximum likelihood algorithm.

E. OBIA Joint Classification

OBIA has the peculiarity of working with multiresolution hierarchical levels; therefore, the integration of multisource data can occur during the OBIA itself.

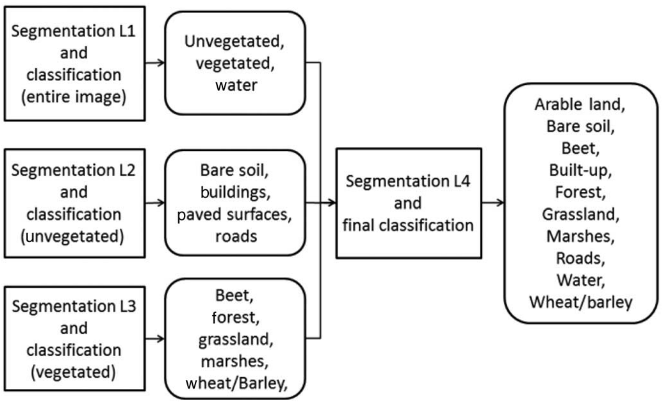

Fig. 7. Workflow of OBIA classification.

TABLE II
SEGMENTATION PARAMETERS USED IN OBIA FOR GE1 AND CSK® DATA

Input layers	L1	L2	L3	L4
Classification of GE1				
GE1 MS1	Yes	Yes	Yes	Yes
GE1 MS2	Yes	Yes	Yes	Yes
GE1 MS3	Yes	Yes	Yes	Yes
GE1 MS4	Yes	Yes	Yes	Yes
Scale	12	16	43	75
Shape	0.4	0.1	0.3	0.4
Compactness	0.6	0.6	0.7	0.9
Starting level	Pixel	L1	L2	L3
Classification of GE1+CSK				
GE1 MS1	Yes	Yes	Yes	Yes
GE1 MS2	Yes	Yes	Yes	Yes
GE1 MS3	Yes	Yes	Yes	Yes
GE1 MS4	Yes	Yes	Yes	Yes
CSK® amplitude	Yes	Yes	Yes	Yes
Contrast 3×3	No	No	No	No
Contrast 7×7	No	No	Yes	Yes
Dissimilarity 3×3	No	No	No	No
Dissimilarity 9×9	No	No	Yes	Yes
Homogeneity 3×3	No	No	No	No
Variance 3×3	No	No	No	No
Variance 11×11	No	No	Yes	Yes
Scale	12	16	43	75
Shape	0.4	0.1	0.3	0.4
Compactness	0.6	0.6	0.7	0.9
Starting level	Pixel	L1	L2	L3

Image segmentation and classification with the nearest neighbor algorithm was performed using four hierarchical levels, according to the flow diagram outlined in Fig. 7 and the input data illustrated in Tables II and III. First, the top-level classes "unvegetated," "vegetated," and "water" were generated using the classification level CL1. Next, the top-level class "unvegetated" was subdivided using the classification level CL2 into "bare soil," "paved surfaces," "buildings," and "roads" and the top-level class "vegetated" was subdivided using the classification level CL3 into "forest," "grassland," "marshes," "beet," and "wheat/barley." Finally, all the LC/LU classes were included in the final classification level CL4.

TABLE III

PARAMETERS USED IN OB JOINT CLASSIFICATION OF GE1 AND CSK® DATA

Classification level	Classes	Features for NN algorithm	
		GE1	GE1+CSK®
CL1 (entire image)	Unvegetated; vegetated; water	Mean GE1 MS1; mean GE1 MS2; mean GE1 MS3; mean GE1 MS4; NDVI	Mean GE1 MS1; mean GE1 MS2; mean GE1 MS3; mean GE1 MS4; NDVI; mean CSK®; mean CSK®; dissimilarity 9×9; mean CSK® contrast 7×7; standard deviation CSK®; dissimilarity 3×3; standard deviation CSK® 11×11; standard deviation CSK®; contrast 3×3
CL2 (unvegetated)	Bare soil; buildings; roads; paved surfaces	Mean GE1 MS1; mean GE2 MS2; mean GE3 MS3; standard deviation GE1 MS3; standard deviation GE1 MS4; compactness; length/width ratio	mean GE1 MS1; mean GE2 MS2; mean GE3 MS3; standard deviation GE1 MS3; standard deviation GE1 MS4; compactness; length/width ratio; mean CSK®; mean CSK® contrast 7×7; standard deviation CSK® dissimilarity 3×3; standard deviation CSK® 11×11; standard deviation CSK® contrast 3×3
CL3 (vegetated)	Grassland; wheat/barley; forest; marshes	Mean GE3 MS4; standard deviation GE1 MS4; NDVI; area; compactness; shape index; distance to objects “water”; border to objects “shadows”; length/width ratio	Mean GE3 MS4; standard deviation GE1 MS4; NDVI; area; compactness; shape index; distance to objects “water”; border to objects “shadows”; length/width ratio; mean CSK®; mean CSK® contrast 7×7; standard deviation CSK® 11×11; standard deviation CSK® contrast 3×3
CL4 (final classification)	Arable land; built-up, roads, grassland, wheat/barley, forest, marshes, water	Existence of sub-objects “bare soil”; existence of sub-objects “buildings”; existence of sub-objects “paved surfaces”; existence of sub-objects “roads”; existence of sub-objects “Grassland”; existence of sub-objects “wheat/barley”; existence of sub-objects “forest”; existence of sub-objects “marshes”; existence of sub-objects “water”; mean GE3 MS4; standard deviation GE1 MS4; length/width ratio	Existence of sub-objects “bare soil”; existence of sub-objects “buildings”; existence of sub-objects :paved surfaces”; existence of sub-objects :roads”; existence of sub-objects “grassland”; existence of sub-objects “wheat/barley”; existence of sub-objects :forest”; existence of sub-objects “marshes”; existence of sub-objects “water”; mean GE3 MS4; standard deviation GE1 MS4; length/width ratio; mean CSK®; standard deviation CK 11×11

The OB classification of GE1 + CSK® data followed the same workflow described for GE1 but with the inclusion of CSK® amplitude values and the following GLCM textural features

$$\text{Homogeneity} = \sum_{i=1}^{N-1} \sum_{j=1}^{N-1} [p(i,j)] \,/\, \left[1 + (i-j)^2\right] \quad (2)$$

$$\text{Contrast} = \sum_{i=1}^{N-1} \sum_{j=1}^{N-1} p(i,j)(i-j)^2 \quad (3)$$

$$\text{Dissimilarity} = \sum_{i=1}^{N-1} \sum_{j=1}^{N-1} p(i,j)\,|i-j| \quad (4)$$

$$\text{Entropy} = \sum_{i=1}^{N-1} \sum_{j=1}^{N-1} p(i,j) \log\left(p(i,j)\right) \quad (5)$$

$$\text{Second Moment} = \sum_{i=1}^{N-1} \sum_{j=1}^{N-1} p(i,j)^2 \quad (6)$$

$$\text{Correlation} = \sum_{i=1}^{N-1} \sum_{j=1}^{N-1} [(i,j)p(i,j) - \mu_i \mu_j] \,/\, [\sigma_i \sigma_j] \quad (7)$$

where μ and σ are mean and standard deviation, i and j are values and coordinates of the cooccurrence matrix, $p(i,j)$ are the normalized frequencies of two neighboring cells with (i,j) values, and N is the size of the cooccurrence matrix.

GLCMs were calculated for CSK® with kernel sizes from 3×3 to 51×51. The most meaningful parameters were determined by analyzing their class separability based on the training samples.

III. RESULTS AND DISCUSSION

A. *Classification Results*

Figs. 8 and 9 show the LC/LU classification maps. Tables IV and V show the overall accuracy (OA), Cohen's k coefficient, user accuracy (UA), and producer accuracy (PA) for all the methods/input data used. The corresponding confusion matrices are summarized in Tables VI–IX.

At pixel level, SAR has much greater variance within each class compared to optical data. Even if preprocessed, CSK® image still showed the classical “salt and pepper” effect, especially in built-up areas where this phenomenon is prominent due to the close alternation of very bright (reflectors) and very dark (SAR shadows) spots. Consequently, when SAR amplitudes are “injected” into the MS images, new information is available for the thematic classification, but the intraclass variability increases to the detriment of the classification accuracy. As a matter of fact, the inclusion of the SAR information did not significantly improve the PB classification: both the OA and the k coefficient only slightly increased to about 1.5%.

More in detail, in a few classes (i.e., “built-up,” “Arable land,” and “wheat”), the PA decreased when including CSK® data, whereas in other cases (i.e., “wheat,” “grassland,” and “marshes”), there was a decrease in UA. For the LC/LU

Fig. 8. Results from PB classification. *Left*: classification map of GE1 data. *Center*: classification map of GE1 and CSK® fused data (data provided by the Italian Space Agency). *Right*: GE1 false color composition.

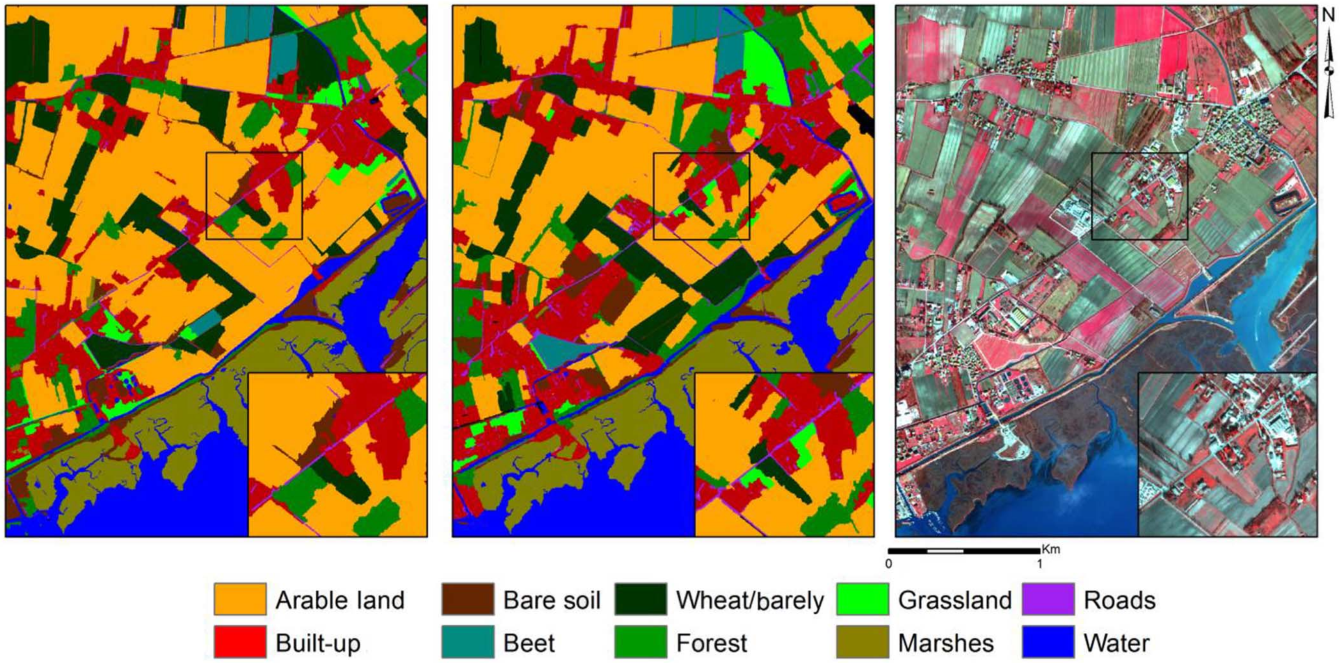

Fig. 9. Results from OB classification. *Left*: classification map of GE1 data. *Center*: classification map of GE1 and CSK® data (data provided by the Italian Space Agency). *Right*: GE1 false color composition.

classes "forest," "bare soil," and "roads," the data fusion led to improvement of the UA and PA.

At object level, once reduced the speckle noise and after log-transformation, clipping, and rescaling, standard image segmentation techniques could be efficiently applied to radar data. In this case, the inclusion of the SAR information and its textural features calculated with GLCMs provided a significant improvement in thematic classification: +21.6% for OA and +25.7% for k coefficient with respect to OBIA of optical data and +29.8% for OA and +35.4% for k coefficient with respect to PB optical classification. The UA and PA increased in near all the LC/LU classes, with the significant exclusion of the classes "grassland" that showed a lower UA and "beet" that showed a lower PA.

To further explore the contribution of the radar data to LC/LU mapping, OBIA was also performed with only CSK® data. In

TABLE IV

OA AND COHEN'S k FOR THE PB AND OB CLASSIFICATIONS OF GE1 AND GE1 + CSK$^{\circledR}$ AND DATA

	GE1 PB	GE1 + CSK$^{\circledR}$ PB	Δ (%)	GE1 OB	GE1 + CSK$^{\circledR}$ OB	Δ (%)
OA	0.684	0.695	+1.6	0.730	0.888	**+21.6**
k	0.65	0.66	+1.5	0.70	0.88	**+25.7**

Best results in bold.

TABLE V

UA AND PA FOR THE PB AND OB CLASSIFICATIONS OF GE1 AND GE1 + CSK$^{\circledR}$ AND DATA

Classes	GE1 PB (%)		GE1+CSK$^{\circledR}$ PB (%)		GE1 OB (%)		GE1+CSK$^{\circledR}$ OB (%)	
	PA	UA	PA	UA	PA	UA	PA	UA
Arable Land	52.5	68.2	42.5	79.4	88.5	41.4	82.5	83.8
Built-up	34.5	56.6	29.5	63.4	65.5	60.1	93.0	79.2
Bare soil	41.0	39.2	64.0	41.7	9.0	36.7	63.0	86.9
Forest	59.0	59.0	62.5	68.7	100.0	94.8	98.0	100.0
Grassland	63.5	85.2	56.5	78.5	84.5	69.3	98.0	74.8
Marshes	85.5	84.7	86.0	84.3	81.5	75.8	97.5	87.8
Roads	87.0	63.5	89.0	69.3	52.5	92.1	82.0	97.0
Water	85.5	100.0	89.0	100.0	99.0	89.6	100.0	91.7
Beet	94.5	93.6	95.0	93.1	53.0	100.0	76.0	95.6
Wheat/ barely	81.5	51.4	80.5	49.7	96.5	99.5	98.0	100.0

Best results in bold.

this case, a single segmentation level was created using the following input layers selected with a trial-and-error approach: mean CSK$^{\circledR}$, mean contrast 7×7, mean dissimilarity 9×9, standard deviation CSK$^{\circledR}$ 11×11. Again, the classification was done using the nearest neighbor algorithm but only into six classes (i.e., "Arable land," "built-up," "water," "marshes," "bare soil," and "vegetated"). The map is shown in Fig. 10. The computed OA was 57.2% and the k coefficient was 0.49, mainly due to the inability to differentiate "marshes" from the other vegetation. Moreover, the misclassification between "bare soil" and "vegetation" was relevant. On the other hand, CSK$^{\circledR}$ data well discriminated built-up areas and water, as expected (Table X). When comparing these results to homologous obtained with GE1 data (Table XI), it is clear that the major contribution of SAR was in increasing the PA of the classes "built-up," and "water" and the UA of the classes "Arable land," "built up," and "water." Nevertheless, also all the other LC/LU classes benefited from the inclusion of the SAR information. A special reference needs to be made for the class "bare soil." Both GE and CSK$^{\circledR}$ individually produced very poor results, but the joint classification led to acceptable values of UA, again confirming that the joint processing of MS and SAR data can extract more information than what can be gathered from the single sensors.

B. *Comparison to Past Studies and New Outcomes*

Past studies suggested that the incorporation of SAR data could improve MS LC/LU mapping. However, as recalled in the introduction, most of the literature considered medium-resolution data, typically Landsat-TM or SPOT for optical and RADARSAT or ERS for radar, whereas only fewer studies focused on the use of high-resolution data that set new issues about the increase of the internal variability of LC/LU classes. Moreover, most of the past studies about OBIA suggested different LU/LC classification approaches for urban and agricultural/natural environments.

With respect to high-resolution SAR and MS data integration, [40] described a study of thematic classification involving optical and radar imagery collected from aircraft on the eastern coast in far north Queensland (Australia). Using CASI images (fourteen 2.5-m spatial resolution narrow spectral bands) and AIRSAR multiband (L-band, P-band, and C-band) multipolarimetric acquisitions (10-m spatial resolution), they found that the combined use of the optical/SAR data set led to an increase of the OA up to 12.4% (from 0.710 to 0.798) for the classification of tropical mangrove ecosystems. Reference [7] reported the improvement of urban land-cover classification using a refined Bayesian classification algorithm with high-resolution QuickBird MS image (four 2.4-m spectral bands) and high-resolution TerraSAR-X dual-polarization acquisition (1-m spatial resolution) imaged over the urban area of Ulaanbaatar (Mongolia). The authors concluded that the joint use of optical and radar data led to an increase of 8.9% for OA (OA $=$ 0.7537) using standard Bayesian maximum likelihood, compared to the classification results of the optical data only (OA $=$ 0.6924). Reference [10] combined high-resolution QuickBird MS data (four 2.4-m spectral bands) and high-resolution single polarization TerraSAR-X Stripmode acquisitions (3.0-m spatial resolution) collected over the urban area of Nanjing (China). Fusing optical and SAR imagery with OBIA, they improved the land-cover classification accuracy by 7.0% for OA (from 0.830 to 0.888) and by 10.4% for k coefficient (from 0.77 to 0.85), with respect to optical-based image classification. Reference [30] analyzed the performance attained by combining optical and SAR single-images into a joint classification. Using the ESA AgriSAR 2009 data set, made up of high-resolution Radarsat-2 fine quad-polarimetric acquisitions (spatial resolution of 5.4 m in slant range and 8.0 m in azimuth direction) and a high-resolution RapidEye MS image (five 6.5-m spectral bands), they highlighted a thematic enhancement in the range of 6%–8%. The authors concluded that, for crop classification, the information complementarity with respect to the optical spectral bands was effectively provided by SAR data, with almost every polarimetric mode (single-pol, dual-pol, and quad-pol). However, the authors pointed out that most of the benefits from multisensor integration concerned only some of the land-cover classes considered. Reference [13] studied the multisensor classification of high-resolution pan-sharpened GE1 image (three 0.5-m spectral bands) and high-resolution single polarization CSK$^{\circledR}$ StripMap acquisition (2.5-m spatial resolution) collected over the port area of Port-au-Prince (Haiti). They described an increase in the classification OA of 4.0% (from 0.7895 to 0.8212) when combining the optical and SAR data. More in details, the authors observed improvements related to the joint use of the CSK$^{\circledR}$ and GE1 images particularly in the urban areas. Finally, [31] tested multisource classification of

TABLE VI
Confusion Matrix for PB Classification of GE1 Data

		Ground truth										
		Arable land	Built-up	Bare soil	Forest	Grassland	Marshes	Roads	Water	Beet	Wheat/ barely	Total
Classification	Arable land	105	8	31	0	0	0	1	0	0	9	154
	Built-up	1	69	9	1	0	0	22	20	0	0	122
	Bare soil	68	10	82	42	0	3	1	0	0	3	209
	Forest	0	31	2	118	3	25	0	1	5	15	200
	Grassland	0	2	2	7	127	0	0	0	4	7	149
	Marshes	0	2	7	21	0	171	1	0	0	0	202
	Roads	4	74	11	1	1	1	174	8	0	0	274
	Water	0	0	0	0	0	0	0	171	0	0	171
	Beet	0	1	0	0	9	0	0	0	189	3	202
	Wheat/ barely	22	3	56	10	60	0	1	0	2	163	317
	Total	200	200	200	200	200	200	200	200	200	200	2000

TABLE VII
Confusion Matrix for PB Classification of GE1 + CSK® Data

		Ground truth										
		Arable land	Built-up	Bare soil	Forest	Grassland	Marshes	Roads	Water	Beet	Wheat/ barely	Total
Classification	Arable land	85	6	8	0	0	0	1	1	0	6	107
	Built-up	0	59	1	0	0	0	15	18	0	0	93
	Bare soil	89	20	128	50	0	6	3	0	0	11	307
	Forest	0	27	0	125	2	20	0	0	2	6	182
	Grassland	0	3	3	10	113	1	0	0	4	10	144
	Marshes	1	9	9	9	0	172	1	1	2	0	204
	Roads	3	72	0	0	2	0	178	2	0	0	257
	Water	0	0	0	0	0	0	0	178	0	0	178
	Beet	0	1	0	0	7	0	0	0	190	6	204
	Wheat/ barely	22	3	51	6	76	1	2	0	2	161	324
	Total	200	200	200	200	200	200	200	200	200	200	2000

TABLE VIII
Confusion Matrix for OB Classification of GE1 Data

		Ground truth										
		Arable land	Built-up	Bare soil	Forest	Grassland	Marshes	Roads	Water	Beet	Wheat/ barely	Total
Classification	Arable land	177	20	129	0	25	28	42	0	7	0	428
	Built-up	0	131	0	0	1	8	8	0	70	0	218
	Bare soil	1	19	18	0	1	0	0	2	3	5	49
	Forest	11	0	0	200	0	0	0	0	0	0	211
	Grassland	11	0	27	0	169	0	30	0	7	0	244
	Marshes	0	25	7	0	4	163	15	0	1	0	215
	Roads	0	3	1	0	0	1	105	0	2	2	114
	Water	0	2	18	0	0	0	0	198	3	0	221
	Beet	0	0	0	0	0	0	0	0	106	0	106
	Wheat/ barley	0	0	0	0	0	0	0	0	1	193	194
	Total	200	200	200	200	200	200	200	200	200	200	2000

random forest in the Llanrhidian salt marsh in Wales (U.K.). For their research, the authors used VHR quad-polarimetric S-band and X-band SAR data (0.75-m spatial resolution in both slant and azimuth direction) imaged with the Astrium Airborne Demonstrator and VHR MS aerial photography (0.25-m spatial resolution for the visible and 0.5-m spatial resolution for the infrared), together with a high-resolution Digital Surface Model derived from a LiDAR survey (2.0-m spatial resolution). The accuracy evaluation of the extent mapping showed an increase in the OA of 3.7% (from 0.8830 to 0.9155) and of the k coefficient of 7.8% (from 0.77 to 0.83) passing from the classification of the optical-based aerial images to all the available data set.

All the above-mentioned studies considered different environments, different land-cover types, and used different source data. Nevertheless, all of them described an improvement in LC/LU classification of about 6%–10% when jointly using optical and radar data. The only exception is reported in [7]. The

TABLE IX

CONFUSION MATRIX FOR OB CLASSIFICATION OF GE1 + CSK® DATA

	Ground truth										
Classification	Arable land	Built-up	Bare soil	Forest	Grassland	Marshes	Roads	Water	Beet	Wheat/ barely	Total
Arable land	165	1	21	0	0	1	0	0	9	0	197
Built-up	1	186	1	0	4	0	20	0	23	0	235
Bare soil	0	0	126	0	0	4	0	0	13	2	145
Forest	0	0	0	196	0	0	0	0	0	0	196
Grassland	34	2	27	0	196	0	3	0	0	0	262
Marshes	0	3	7	0	0	195	13	0	3	1	222
Roads	0	1	0	4	0	0	164	0	0	0	169
Water	0	0	18	0	0	0	0	200	0	0	218
Beet	0	6	0	0	0	0	0	0	152	1	159
Wheat/ barely	0	0	0	0	0	0	0	0	0	196	196
Total	200	200	200	200	200	200	200	200	200	200	2000

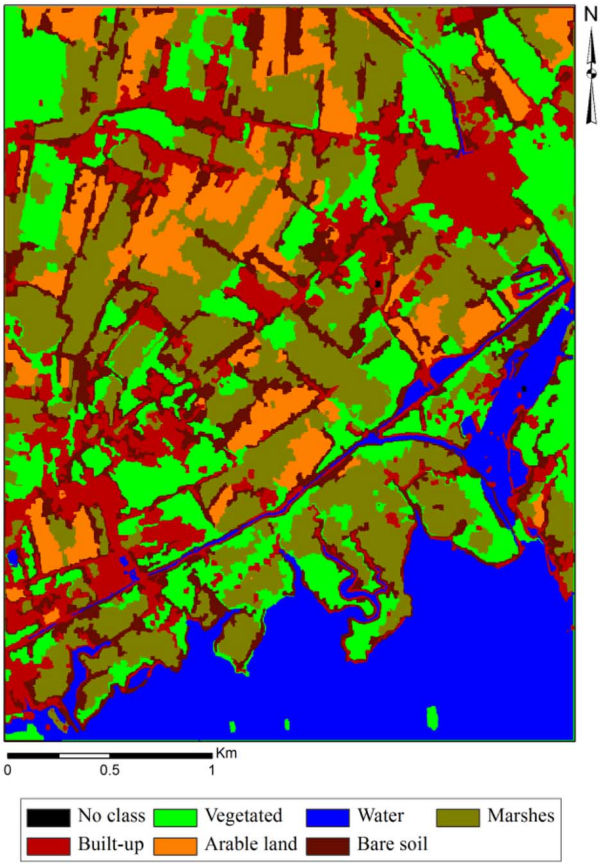

Fig. 10. OB classification of CSK® data (data provided by the Italian Space Agency) into a six-class thematic map.

authors claimed a surprising $+31.4\%$ for OA $(\text{OA} = 0.9096)$ but achieved in the simple classification of an urbanized area (into the following classes: "built-up area," "ger area," "open area," "road," "central squire," and "ice") and, especially, using a priori local knowledge of the study area in the classification workflow, thus, with detriment toward the generalization of the method, making it unlikely suitable for LC/LU mapping of other urban areas.

Our study confirmed that the integration of optical and radar data improves the LC/LU classification, but, with comparison to previous papers, a substantial increase in thematic accuracy was reached (about 20%–25%). Moreover, this study highlighted that OBIA methods are more suitable for data integration rather than PB image fusion techniques, and that also complex environments with a mixture of urban, agricultural, and natural areas can be managed into a unique classification process. With respect to the segmentation of data, some new researches concluded that it is often not appropriate to apply traditional segmentation methods to high-resolution SAR data as they are and propose new segmentation strategies [41]–[43]. On the contrary, our research pointed out that, with appropriate preprocessing, traditional OBIA could also be applied to X-band SAR data without the need of developing *ad hoc* algorithms.

C. *Issues and Possible Improvements*

The workflow described in Fig. 6 contains some arbitrary choices related to data preprocessing, selection of the classifier, and input features. Regarding the preprocessing, our study highlighted that standard radar preprocessing (i.e., focusing, despeckling, equalization, and projected) is not enough when merging together optical images and SAR amplitudes, and the latter needs further processing (i.e., data compression, clipping, and dynamic range rescaling) for making it suitable for the integration with MS images. Besides, the use of despeckle filters and the different viewing angles of the radar sensors with respect to the optical could compromise the high spatial detail of the SAR data. Thus, it is suggested to test the filtered radar data over homogeneous areas to confirm that they can be properly used at the original spatial resolution. If despeckling methods may have a significant influence on PB algorithms, and this should partially explain why CSK® data did not enhance to the maximum likelihood classification of GE1, they have a smaller relevance when using the OBIA approach. This is because OBIA is applied to image objects and not at the pixel level. In particular, the use of different despeckling algorithms has a limited impact on the computation of GLCMs, thus on image classification. On the other hand, it may be nonnegligible for image segmentation.

Regarding the classification algorithm used for PB LC/LU mapping, we adopted one of the (still) most used methods for MS images: maximum likelihood. Several recent comparative studies affirm that the maximum likelihood classifier often yields to higher accuracy and lower errors in per-pixel image

TABLE X

UA AND PA FOR CSK$^{\circledR}$ SIX-CLASSES LC/LU MAP

Class	PA (%)	UA (%)
Built-up	76.0	77.6
Vegetated	47.5	29.9
Water	80.5	99.4
Marshes	54.0	35.9
Arable land	56.5	95.0
Bare soil	28.5	54.8

TABLE XI

UA AND PA FOR GE1 SIX-CLASSES LC/LU MAP

Class	PA (%)	UA (%)
Built-up	45.9	88.5
Vegetated	61.2	67.0
Water	36.7	9.0
Marshes	93.2	84.5
Arable land	81.5	81.5
Bare soil	89.6	99.0

classification of MS images [44]–[48]. Even if the outcomes of past studies may be questionable and different classification algorithms may lead to higher accuracy in specific contexts, in our research, we adopted the same classification scheme (i.e., algorithm, training samples, and testing samples) for both the PB LC/LU mapping. Consequently, results are consistent and the very small differences found in MS versus MS + radar PB thematic mapping are to be ascribed to the additional information included in the radar data.

Regarding the OBIA approach, the input features were selected by including in the data processing only the most meaningful GLCM textural features determined with a sensitivity analysis [17]. Even if the results discussed above showed that a substantial increase in thematic accuracy can be achieved using standard OBIA applied to high-resolution optical and radar data, we should remember that these outcomes were obtained for a single test site. Moreover, this study used only data from single-channel SAR, whereas the inclusion of a multipolarized SAR could bring some polarimetry parameters (e.g., entropy, mean backscattering angle) in the data fusion, thus leading to a higher level of both OA and k coefficient.

Another limit of the study is that the classification maps are referred to the acquisition time of both optical and SAR data only and are not extended to the multitemporal domain, as would be required for a proper knowledge of the temporal evolution of the landscape. Nevertheless, results pointed out that the joint use of VHR optical and SAR images can be quite useful to have a best knowledge of the land fragmentation of the territory, thus increasing the quality of the LC/LU maps generated with VHR optical images. Obviously, the radar technology can collect images all-weather and is not limited by cloudiness, especially during winter; thus, it is possible to think about the use of SAR data only instead of optical data for understanding rapid landscape changes. However, this topic is outside the scopes of our research.

IV. CONCLUSION

This study demonstrated how optical (GE1) and radar (CSK$^{\circledR}$) data imaged with high spatial resolution can be used together for mapping a complex environment with mixture of settlements, cultivations, channels, roads, and marshes using standard OBIA.

Past studies mainly focused on the integration of medium-resolution data and only few papers about high-resolution and VHR data assimilation are available today. The high spatial detail of metric and submetric sensors introduces issues related to the increase of the internal variability of LC/LU classes that may lead to an overall decrease in the mapping accuracy with traditional PB classification.

The major findings of this research are related to the classification techniques and the map accuracy. Regarding the methods, the research demonstrated that an appropriate preprocessing of the SAR data is required for being able to use standard algorithms and techniques traditionally used with optical images, with the great advantage of never requiring the development of *ad hoc* data processing. Regarding the contribution of the SAR signal to optical-based LC/LU thematic classification, validation clearly showed that the inclusion of the SAR information provided a significant improvement in thematic classification in the range of 20%–30% for OA and 25%–35% for k coefficient. It is much more than what was reported in the previous studies. Besides, no distinction was made in managing urban areas and natural areas in the same classification workflow.

In conclusion, this study proved that the integration of VHR MS and X-band SAR data with standard OBIA can considerably improve the LC/LU classification. Thus, metric X-band SAR data could be efficaciously used for providing additional structural information to complement VHR optical images collected by today's satellite systems. Additional research will be required for evaluating the effects of different despeckling techniques on SAR segmentation/classification and layover/shadowing effects in complex topographic sites.

ACKNOWLEDGMENT

The authors would like to thank Prof. C. Prati (Politecnico di Milano) and Tele-Rilevamento Europa (TRE) for the preprocessing of the COSMO-SkyMed data.

REFERENCES

[1] CEOS (2014). The Committee on Earth Observation Satellite's Earth Observation Handbook [Online]. Available: http://www.eohandbook.com

[2] C. Castañeda and D. Ducrot, "Land cover mapping of wetland areas in an agricultural landscape using SAR and Landsat imagery," *J. Environ. Manage.*, vol. 90, no. 7, pp. 2270–2277, 2009.

[3] H. McNairn, C. Champagne, J. Shang, D. Holmstrom, and G. Reichert, "Integration of optical and synthetic aperture radar (SAR) imagery for delivering operational annual crop inventories," *ISPRS J. Photogramm. Remote Sens.*, vol. 64, no. 5, pp. 434–449, 2009.

[4] S. Huang, C. Potter, R. L. Crabtree, S. Hager, and P. Gross, "Fusing optical and radar data to estimate sagebrush, herbaceous, and bare ground cover in Yellowstone," *Remote Sens. Environ.*, vol. 114, no. 2, pp. 251–264, 2010.

[5] N. Pierdicca, M. Chini, and F. Pelliccia, “The contribution of SIASGE radar data integrated with optical images to support thematic mapping at regional scale,” *IEEE J. Sel. Topics Appl. Earth Observ. Remote Sens.*, vol. 7, no. 7, pp. 2821–2833, Jul. 2014.

[6] C. Bignami *et al.*, “Multisensor satellite monitoring of the 2011 Puyehue-cordon Caulle eruption,” *IEEE J. Sel. Topics Appl. Earth Observ. Remote Sens.*, vol. 7, no. 7, pp. 2786–2796, Jul. 2014.

[7] D. Amarsaikhan *et al.*, “Fusing high-resolution SAR and optical imagery for improved urban land cover study and classification,” *Int. J. Image Data Fusion*, vol. 1, no. 1, pp. 83–97, 2010.

[8] M. Gianinetto *et al.*, “Fusione di dati COSMO-SkyMed e Geoeye-1 per la classificazione del land cover nella laguna di Venezia,” in *Proc. 15th Conferenza Nazionale ASITA*, Colorno, Italy, 2011, pp. 1171–1182.

[9] F. Palazzo *et al.*, “An application of COSMO-SkyMed to coastal erosion studies,” *Eur. J. Remote Sens.*, vol. 45, pp. 361–370, 2012.

[10] Y. Luo *et al.*, “A novel classification method based on texture analysis using high-resolution SAR and optical data,” in *Proc. 2nd Int. Workshop Earth Observ. Remote Sens. Appl.*, 2012, pp. 1–5.

[11] M. Rusmini *et al.*, “High-resolution SAR and high-resolution optical data integration for sub-urban land-cover classification,” in *Proc. Int. Geosci. Remote Sens. Symp. (IGARSS)*, Munich, Germany, 2012, pp. 4986–4989.

[12] F. Braga, L. Tosi, C. Prati, and L. Alberotanza, “Shoreline detection: Capability of COSMO-SkyMed and high-resolution multispectral images,” *Eur. J. Remote Sens.*, vol. 46, pp. 837–853, 2013.

[13] A. Voisin, V. A. Krylov, G. Moser, S. B. Serpico, and J. Zerubia, “Supervised classification of multisensor and multiresolution remote sensing images with a hierarchical copula-based approach,” *IEEE Trans. Geosci. Remote Sens.*, vol. 52, no. 6, pp. 3346–3358, Jun. 2014.

[14] A. P. Cracknell, “Review article synergy in remote sensing-what’s in a pixel?,” *Int. J. Remote Sens.*, vol. 19, no. 11, pp. 2025–2047, 1998.

[15] P. Aplin, P. M. Atkinson, and P. J. Curran, “Fine spatial resolution simulated satellite sensor imagery for land cover mapping in the United Kingdom,” *Remote Sens. Environ.*, vol. 68, no. 3, pp. 206–216, 1999.

[16] T. Blaschke, “Object based image analysis for remote sensing,” *ISPRS J. Photogramm. Remote Sens.*, vol. 65, pp. 2–16, 2010.

[17] M. Gianinetto *et al.*, “Hierarchical classification of complex landscape with VHR pan-sharpened satellite data and OBIA techniques,” *Eur. J. Remote Sens.*, vol. 47, pp. 229–250, 2014.

[18] T. Ceccarelli *et al.*, “Land cover data from Landsat single-date imagery: An approach integrating pixel-based and object-based classifiers,” *Eur. J. Remote Sens.*, vol. 46, pp. 699–717, 2013.

[19] P. Maianti *et al.*, “Monitoring large oil slick dynamics with moderate resolution multispectral satellite data,” *Nat. Hazards*, vol. 73, pp. 473–492, 2014.

[20] S. Bhaskaran, S. Paramananda, and M. Ramnarayan, “Per-pixel and object-oriented classification methods for mapping urban features using Ikonos satellite data,” *Appl. Geogr.*, vol. 30, no. 4, pp. 650–665, 2010.

[21] Y. Chen, W. Su, J. Li, and Z. Sun, “Hierarchical object oriented classification using very high resolution imagery and LIDAR data over urban areas,” *Adv. Space Res.*, vol. 43, no. 7, pp. 1101–1110, 2009.

[22] M. Machala and L. Zejdová, “Forest mapping through object-based image analysis of multispectral and LiDAR aerial data,” *Eur. J. Remote Sens.*, vol. 47, pp. 117–131, 2014.

[23] C. J. van der Sande, S. M. de Jong, and A. P. de Roo, “A segmentation and classification approach of IKONOS-2 imagery for land cover mapping to assist flood risk and flood damage assessment,” *Int. J. Appl. Earth Observ. Geoinf.*, vol. 4, no. 3, pp. 217–229, 2003.

[24] R. Mathieu, C. Freeman, and J. Aryal, “Mapping private gardens in urban areas using object-oriented techniques and very high-resolution satellite imagery,” *Landscape Urban Plann.*, vol. 81, no. 3, pp. 179–192, 2007.

[25] O. Shiro, “Land cover classification based on image objects for high resolution satellite image,” *Southeast Asian Stud.*, vol. 46, no. 4, pp. 578–592, 2008.

[26] K. Johansen, N. C. Coops, S. E. Gergel, and Y. Stange, “Application of high spatial resolution satellite imagery for riparian and forest ecosystem classification,” *Remote Sens. Environ.*, vol. 110, no. 1, pp. 29–44, 2007.

[27] W. Su *et al.*, “Textural and local spatial statistics for the object-oriented classification of urban areas using high resolution imagery,” *Int. J. Remote Sens.*, vol. 29, no. 11, pp. 3105–3117, 2008.

[28] F. Del Frate, F. Pacifici, G. Schiavon, and C. Solimini, “Use of neural networks for automatic classification from high-resolution images,” *IEEE Trans. Geosci. Remote Sens.*, vol. 45, no. 4, pp. 800–809, Apr. 2007.

[29] F. Pacifici, M. Chini, and W. J. Emery, “A neural network approach using multi-scale textural metrics from very high-resolution panchromatic imagery for urban land-use classification,” *Remote Sens. Environ.*, vol. 113, no. 6, pp. 1276–1292, 2009.

[30] L. Iannini, R. A. Molijn, and R. F. Hanssen, “Integration of multispec-tral and C-band SAR data for crop classification,” in *Proc. Remote Sens. Agric. Ecosyst. Hydrol. XV*, 2013, vol. 8887, 88871D, pp. 1–8.

[31] S. van Beijma, A. Comber, and A. Lamb, “Random forest classification of salt marsh vegetation habitats using quad-polarimetric airborne SAR, elevation and optical RS data,” *Remote Sens. Environ.*, vol. 149, pp. 118–129, 2014.

[32] F. Caltagirone *et al.*, “The COSMO-SkyMed dual use earth observation program: Development, qualification, and results of the commissioning of the overall constellation,” *IEEE J. Sel. Topics Appl. Earth Observ. Remote Sens.*, vol. 7, no. 7, pp. 2754–2762, Jul. 2014.

[33] J. de Gruijter, “Spatial sampling schemes for remote sensing,” in *Remote Sensing and Digital Image Processing: Spatial Sampling Schemes for Remote Sensing*. Norwell, MA, USA: Kluwer, 2002, 284 pp.

[34] J. Radoux and P. Bogaert, “Accounting for the area of polygon sampling units for the prediction of primary accuracy assessment indices,” *Remote Sens. Environ.*, vol. 142, pp. 9–19, 2014.

[35] M. J. Canty, *Image Analysis, Classification and Change Detection in Remote Sensing with Algorithms for ENVI/IDL*, 2nd ed. New York, NY, USA: Taylor & Francis, 2009.

[36] A. Ferretti, C. Prati, and F. Rocca, “Permanent scatterers in SAR interferometry,” *IEEE Trans. Geosci. Remote Sens.*, vol. 39, no. 1, pp. 8–20, Jan. 2001.

[37] A. Ferretti *et al.*, “A new algorithm for processing interferometric data-stacks: SqueeSAR,” *IEEE Trans. Geosci. Remote Sens.*, vol. 49, no. 9, pp. 3460–3470, Sep. 2011.

[38] Z. Wang, D. Ziou, C. Armenakis, D. Li, and Q. Li, “A comparative analysis of image fusion methods,” *IEEE Trans. Geosci. Remote Sens.*, vol. 43, no. 6, pp. 1391–1402, Jun. 2005.

[39] V. Karathanassi, P. Kolokousis, and S. Ioannidou, “A comparison study on fusion methods using evaluation indicators,” *Int. J. Remote Sens.*, vol. 28, no. 10, pp. 2309–2341, 2007.

[40] A. Held, C. Ticehurst, L. Lymburner, and N. Williams, “High resolution mapping of tropical mangrove ecosystems using hyperspectral and radar remote sensing,” *Int. J. Remote Sens.*, vol. 24, no. 13, pp. 2739–2759, 2003.

[41] H. Yu, X. Zhang, S. Wang, and B. Hou, “Context-based hierarchical unequal merging for SAR image segmentation,” *IEEE Trans. Geosci. Remote Sens.*, vol. 51, no. 2, pp. 995–1009, Feb. 2013.

[42] D. Yang, L. Wang, X. Hei, and M. Gong, “An efficient automatic SAR image segmentation framework in AIS using kernel clustering index and histogram statistics,” *Appl. Soft Comput.*, vol. 16, pp. 63–79, 2014.

[43] D. Xiang, T. Tang, C. Hu, Y. Li, and Y. Su, “A Kernel clustering algorithm with fuzzy factor: Application to SAR image segmentation,” *IEEE Geosci. Remote Sens. Lett.*, vol. 11, no. 7, pp. 1290–1294, Jul. 2014.

[44] M. E. Hodgson, J. R. Jensen, J. A. Tullis, K. D. Riordan, and C. M. Archer, “Synergistic use of Lidar and color aerial photography for mapping urban parcel imperviousness,” *Photogramm. Eng. Remote Sens.*, vol. 69, no. 9, pp. 973–980, 2003.

[45] M. B. Patil, C. G. Desai, and B. N. Umrikar, “Image classification tool for land use/land cover analysis: A comparative study of maximum likelihood and minimum distance method,” *Int. J. Geol. Earth Environ. Sci.*, vol. 2, no. 3, pp. 189–196, 2012.

[46] A. Ahmad, “Analysis of maximum likelihood classification on multispectral data,” *Appl. Math. Sci.*, vol. 6, no. 129, pp. 6425–6436, 2012.

[47] P. Du *et al.*, “Multiple classifier system for remote sensing image classification: A review,” *Sensors*, vol. 12, pp. 4764–4792, 2012.

[48] P. P. Sisodia, V. Tiwari, and A. Kumar, “Analysis of supervised maximum likelihood classification for remote sensing image,” in *Proc. IEEE Int. Conf. Recent Adv. Innov. Eng. (ICRAIE’14)*, Jaipur, India, 2014, pp. 1–4.